1 # Sensitivity of the Distribution of Thunderstorms to

2 # Sea Surface Temperatures in Four Australian East

3 # Coast Lows

4

5

6 Christopher R. S. Chambers

7 School of Earth Sciences, University of Melbourne, Parkville, Australia

8

9 Gary B. Brassington

10 Centre for Australian Weather and Climate Research, Bureau of Meteorology, Sydney,

11 Australia

12

13 Kevin Walsh

14 School of Earth Sciences, University of Melbourne, Parkville, Australia

15

16 Ian Simmonds

17 School of Earth Sciences, University of Melbourne, Parkville, Australia

18

19

20 _____

21 *Corresponding author address:* Kevin Walsh, School of Earth Sciences, University of Melbourne 3010,

22 Victoria, Australia.

23 E-mail: kevin.walsh@unimelb.edu.au

24 Tel: 61 (0)3 8344 6523

Abstract

The relationship between the sea surface temperature (SST) distribution and the locations of thunderstorms during four Australian east coast lows is investigated using both lightning observations and numerical simulation results. The focus is placed on investigating changes in convective instability caused by the introduction of complex, high-resolution ocean eddy and frontal structures present in Bluelink SST datasets. Global Position and Tracking System lightning data are overlaid on maps of SST to investigate whether a thunderstorm-SST relationship is discernible. Weather Research and Forecast model simulations are used to establish what atmospheric changes contribute to the observed distributions of thunderstorms. Maximum convective available potential energy (MCAPE) analysis shows a distinct relationship to the SST distribution. In particular areas of elevated MCAPE are related to regions of warmer SST with horizontal advection often displacing increased MCAPE downwind of the warmer SST. At short timescales of 3 to 6 hours, the differences in MCAPE become larger and more localized and show a strong correlation with the observed lightning. This suggests that at times the thunderstorms are directly related to the complex structures in the detailed SST dataset. For the damaging Pasha Bulker case the plume of thunderstorms associated with the coastal damage occurs downwind of the region of enhanced MCAPE on the southern flank of the warm eddy. Based on these results it is concluded that the particular features of the warm eddy enhanced the thunderstorm potential over the coastal region during this event and helped in localising the area of greatest impact for thunderstorm related intense rainfall.

1. Introduction

Australian east coast lows (ECLs) or east coast cyclones (Bridgman 1985, Holland et al. 1987, McInnes et al. 1992, Qi et al. 2006, Browning and Goodwin 2013, Dowdy et al. 2013a, b, Pepler et al. 2014) are subtropical low pressure weather systems that tend to develop rapidly over the oceanic region where the warm East Australian Current (EAC) flows southward off the east coast of Australia. ECLs can have characteristics of both tropical and extratropical cyclones (Evans and Guishard 2009) and are thought to develop through both baroclinic instability and diabatic heating related instabilities (Hart 2003).

ECLs have historically been responsible for major flooding events, damage to coastal infrastructure, and the wrecking and beaching of multiple ships including the Norwegian bulk carrier the Sygna in May 1974 (Bridgeman 1986) and the bulk carrier Pasha Bulker in June 2007 (Mills et al. 2010). ECLs are notoriously difficult to forecast, in part because of their tendency to rapidly intensify overnight. In addition, features within these storms, such as thunderstorm bands, can localize the impact, increasing further the complications in producing an accurate forecast. Ocean eddies in the EAC produce a complicated sea surface temperature (SST) distribution that affects the rainfall distribution and coastal impacts from ECLs (Chambers et al. 2014). This work expands on Chambers et al. by investigating whether the distribution of thunderstorms within three additional ECLs are related to the SST distribution.

On the large scale, ECLs typically develop under consistent upper and lower-level atmospheric patterns. The lower-atmospheric pattern is a low or trough in the subtropical easterly flow known as an "easterly dip" (Fandry and Leslie 1984) that has a ridge on its poleward side. ECLs can develop when an easterly dip develops under, or to the east of, a mid-tropospheric cold-core cyclone or trough in the upper tropospheric westerlies. The cold pools and associated cut-off cyclones present at the beginning of each of the four ECLs in

3

71   this study are shown in Figure 1. As the pool of cold air moves eastward, it passes from

72   relatively dry continental Australia to the warm moist air mass present over the warm waters

73   of the EAC. The presence of cold air above warm moist low level air leads to an increase in

74   vertical buoyant instability making the troposphere more favourable for deep convection.

75   The EAC is a western boundary current of the South Pacific sub-tropical gyre that

76   propagates poleward along the east coast of Australia (Figure 2). The EAC transports warm

77   tropical water from the Coral Sea poleward to the Tasman Sea and has a much greater eddy

78   kinetic energy than other western boundary currents (Hamon, 1965; Stammer, 1997;

79   Brassington et al., 2011). Consequently, anticyclonic warm eddies of the order of 250 km

80   diameter are shed from the current near $32°$ S. The warm eddies can have a mixed layer depth

81   exceeding 300 m in their core (Andrews and Scully-Power 1976) and their rotation and deep

82   vertical structure resists cooling of the eddy interior. As warm eddies move southward they

83   enter a progressively cooler ocean environment leading to the development of localised

84   regions of strong SST gradients.

85   SST gradients have been found to impact the overlying atmosphere in a number of

86   ways that could influence thunderstorm development. In regions of large SST gradients

87   which occur near meandering ocean currents such as the EAC, previous research has shown a

88   strong positive correlation between SST and surface wind speed perturbations at spatial

89   scales of between 100 and 1000 km (see the review by Small et al. 2008).

90   Radar observations of a persistent area of rain over the Gulf Stream led Hobbs (1987)

91   to introduce the concept of a 'Gulf Stream rainband'. Warner et al. (1990) found that sharp

92   SST gradients in the vicinity of the Gulf Stream triggered convergence in the lower

93   troposphere. The Gulf Stream rainband has been associated with rapidly developing

94   thunderstorms (Trunk and Bosart, 1990, Christian et al., 2003, Li et al., 2004) and convective

95   precipitation has been found to be sensitive to SST gradients along the flanks of the Gulf

96   Stream (Kuwano-Yoshida et al. 2010).

97   Recent studies have confirmed that modifications of lower-tropospheric flow by

98   mesoscale SST gradients can translate upward and can trigger or enhance atmospheric

99   convection (Minobe et al. 2008; Vianna et al. 2010; Xu et al. 2011; Li and Carbone 2012).

100   Miyama et al. (2012) found that a convective rainband over the Kuroshio Current was

101   successfully simulated only when a high resolution SST dataset was prescribed. Modelling

102   experiments incorporating smoothed SST fronts in the East China Sea have been completed

103   by Xu et al. (2011) and Tanimoto et al. (2011) and have demonstrated the importance of

104   incorporating detailed SSTs to generate accurate weather simulations. By comparing

105   smoothed SST with high-resolution SST simulations of a Baiu rain event over the Kuroshio,

106   Sasaki et al. (2012) demonstrated that the convective available potential energy (CAPE)

107   difference between the simulations was positively correlated with the SST difference. The

108   increased CAPE was attributed to increased equivalent potential temperature in the boundary

109   layer from enhanced surface fluxes off the warmer ocean surface.

110   While previous research has established these important results concerning the role of

111   SST gradients on the atmosphere, the dependence of the response on conditions in the

112   atmosphere has not been extensively studied. The vertical mixing of momentum will depend

113   on the vertical wind shear and buoyancy in the lower troposphere, as well as on storm

114   features such as regions of convergence and convection. An ECL is often associated with

115   unstable conditions and complicated vertical wind shear distributions because of the typical

116   presence of a cold-core mid-level cyclone propagating across the warm EAC. It is unknown

117   how this will affect the SST-atmospheric response. In addition, previous research has been

118   primarily concerned with timescales of days or longer but in an ECL the significant damaging

119   weather usually occurs on timescales of hours. Therefore, for the purpose of forecasting, it is

120   of paramount interest to determine how these SST gradient responses develop on shorter

121   timescales during these damaging storm events to determine if they play a significant role.

122   This study compares observed lightning with simulated CAPE, two factors that have

123   been found to be related in past studies. Larger CAPE has been associated with the potential

124   for more vigorous convection which promotes more lightning (Williams et al. 1992; Rutledge

125   et al. 1992). Williams et al. found that during transition from a break period to the monsoon

126   over Darwin the lightning yield decreased by more than an order of magnitude for a halving

127   of CAPE. This corresponds to a decrease in CAPE of the order 1000 Jkg^{-1} which was in turn

128   found to be equivalent to a decrease in surface wet-bulb temperature of about 1 °C. Buechler

129   et al. (1994) noted a similar sensitivity for mid-latitude thunderstorms. Additionally, several

130   studies have found correlations between lightning and precipitation rate (Alexander et al

131   1999; Chang et al. 2001; Pessi and Businger 2009). While thunderstorms occurring in an

132   environment with larger CAPE would be expected to have more lightning, there are other

133   critical factors that will influence the occurrence and intensity of a lightning producing

134   thunderstorm, such as adequate moisture through the troposphere, vertical wind shear, and

135   some form of trigger.

136   The rate of lightning strikes has been found to be positively correlated with the

137   strength of convection (Orville and Vonnegut 1974; Orville et al. 1983; Williams et al. 1992).

138   In the case of tropical cyclones (TCs) there have been a number of investigations into the

139   potential relationship between intensification and the distribution and rate of lightning strikes.

140   Black and Hallet (1999) concluded that generally weak vertical velocities within the eyewall,

141   combined with few supercooled water droplets, limits charge separation and consequently

142   leads to sparse lightning in TC cores. A greater likelihood of eyewall lightning in strong TCs

143   was found by Cecil and Zipser (1999) and greater inner-core lightning during intensification

144   by Squires and Businger (2008) and Abarca and Corbosiero (2011). DeMaria et al. (2012)

145 also found intensifying TCs to have greater lightning density than weakening ones, however

146 the largest lightning densities were found in sheared storms that do not intensify much. They

147 also concluded that inner-core lightning outbreaks can be a signal that an intensification

148 period is coming to an end.

149   With these considerations in mind, we focus on ECLs, using the lightning data to

150 compare with model data to investigate whether the distribution of the thunderstorms is

151 sensitive to the SST initialisation. Lightning data provides a useful source of information for

152 the location of thunderstorms particularly in remote ocean areas that are partially or totally

153 beyond the range of weather radar. The paper will look at the sensitivity of atmospheric

154 instability to changing the SST from a coarse dataset to an ocean eddy resolving dataset. It

155 will investigate this sensitivity at 48-hour, 12-hour, and 3-hour timescales and compare the

156 sensitivity with the observed distribution of lightning.

157   The investigation is presented as follows. Section 2 describes the four ECL case studies

158 and methodology, section 3 presents the simulation and lightning data analysis results, with

159 the discussion in section 4 and the overall conclusions in section 5.

160 **2. Case studies and method**

161   Four ECL case studies have been chosen for this study, two in 2007 and two in 2012. A

162 justification for analysing four contrasting examples is to get a more comprehensive

163 understanding of the relationships between the SST, convection and lightning. The first case

164 (JUN07a) covers the period from 1200 UTC 6 to 0000 UTC 9 June 2007. This event caused

165 over $1.5 billion in damages and led to the beaching of the bulk carrier, the Pasha Bulker at

166 2315 UTC 7 June (0915 EST 8 June) on Nobbys Beach in Newcastle, New South Wales.

167 The low had a wide and persistent band of strong onshore winds associated with a strong

168 pressure gradient on its southern side (Figure 3a) that was responsible for the generation of

169 very rough seas, with the Sydney wave-rider buoy (33.8° S 151.4° E) recording 14.1 m

170 maximum wave heights. From 0200 UTC (1200 EST) to 1600 UTC 8 June (0200 EST 9

171 June), a long lasting, slowly southward propagating, east-west oriented thunderstorm

172 rainband moved onshore in the Newcastle area, leading to very high and localized rainfall.

173 Within this rainband, an intense mesoscale low pressure developed offshore and moved

174 onshore at 1500 UTC 8 June (0100 EST 9 June). In the ocean, a large warm eddy was present

175 centred at 33° S, 155° E as shown in Figure 4a. The sensitivity of rainfall to the introduction

176 of eddy-resolving SSTs has been investigated in Chambers et al. (2014) and they concluded

177 that the presence of a large warm eddy led to a marked enhancement in rainfall along its

178 southern flank. The more detailed SST specifications also produced a better agreement with

179 coastal observations.

180 The second case (JUN07b) occurred several days later in a similar location. The almost

181 stationary low developed near the coast between 1200 UTC 15 June and 1200 UTC 16 June

182 before moving offshore. The minimum sea level pressure reached for this system was 1003

183 hPa at 0600 UTC 17 June, as shown in Figure 3b. Impacts were less than in the JUN07a case

184 although snow over higher ground did lead to the accumulation of 30 cm south of

185 Bungendore (35.25° S, 149.45° E, location marked on Figure 4a). It has been chosen to

186 compare with the first case because the position of a warm ocean eddy had not moved a large

187 distance in the period between the two storms, as can be seen by comparing Figure 4a and b.

188 In the APR12 case, a low pressure system developed rapidly off the south-eastern coast of

189 Australia from 24 to 25 April, 2012. The Australian Bureau of Meteorology (BOM) analysis

190 shows a pressure drop of 6 hPa in 6 hours from 0000 UTC 25 April 2012 to 995 hPa (Figure

191 3c). A MODIS pass at 0325 UTC 15 April (not shown) showed a clearly defined cyclone

192 with multiple deep convective rainbands. Despite the impressive nature of this ECL, there

193   were no significant noted impacts, mainly due to a north-eastward track that took it away

194   from the coast.

195   The JUN12 case was another ECL that developed near the southeast corner of

196   Australia on 4 June 2012. This time the low moved towards the coast before moving rapidly

197   north along the coast. According to the BOM sea level pressure analyses the central pressure

198   dropped 12 hPa between 0000 and 0600 UTC 4 June to 986 hPa (Figure 3d). This ECL

199   brought strong winds and heavy rain to southeast New South Wales. The highest wind gust

200   recorded was 128 km h^{-1} at Wattamolla at 3:30 pm 5 June, while 13.8 metre waves were

201   recorded at Sydney.

202   **Model setup**

203   The four ECLs described above are simulated using the Weather Research and

204   Forecasting (WRF) Model version 3.3.1 (Skamarock et al. 2005). Two domains on a Lambert

205   conformal grid, with resolutions of 15 and 3 km, are used for the simulations, as shown in

206   Figure 2, with different domain locations for the 2007 and 2012 cases. The central grid point

207   is shifted so that the inner domain lies over the region of ECL formation. The outer domain is

208   221 by 171 grid points (3315 km by 2565 km) and the inner domain is 301 by 261 grid points

209   (903 km by 783 km). Fifty five levels are used in the vertical with a model top at 30 hPa. One

210   degree National Centers for Environmental Prediction (NCEP) Final (FNL) Analysis data

211   (Global Climate and Weather Modeling Branch 2003) is used to initialize the atmosphere in

212   the model.

213   The Thompson et al. (2004) microphysics scheme, which contains six water classes

214   (water vapor, cloud water, rain, snow, graupel, and cloud ice) is used. The Betts-Miller-Janjic

215   (Betts and Miller 1986; Janjic 1994) cumulus scheme is used only on the outer domain, with

216   the inner domain calculating the cumulus processes explicitly. Explicit depiction of

217   convection at 3-km resolution is thought to be sufficient to resolve mesoscale convective

218   features (Weisman et al. 1997). Other physics schemes used are the Yonsei University

219   planetary boundary layer parameterization, the Monin–Obukhov surface layer scheme (Hong

220   et al. 2006), the Dudhia (1989) short wave radiation scheme, and the Rapid Radiative

221   Transfer Model for long wave radiation with six molecular species (Mlawer et al. 1997).

222   Two 60-hour simulations are conducted for each of the four ECLs that are identical

223   except for the SST data used as input. The first 12 hours of the simulations are considered a

224   "spin-up" period during which the results are not analysed. The simulation names, integration

225   periods, and SST configurations used are summarised in Table 1. For all cases the SST

226   evolves on a 6-hourly basis to match the atmospheric data input period. The first of the SST

227   configurations (Skin) is the 1 degree resolution skin temperature from the NCEP FNL data

228   that are derived from the Global Data Assimilation System (GDAS). As the middle column

229   of Figure 4 shows, this dataset does not resolve any eddy variability in the EAC on domain 2.

230   The second configuration is for the 2007 cases and uses Bluelink ReANalysis

231   (BRAN, Schiller et al. 2008) SST. BRAN uses SST data from an eddy-resolving ocean model

232   simulation using the Modular Ocean Model (MOM, Griffies et al. 2004) which is constrained

233   through the data assimilation of altimetry, SST and in situ profiles using the Bluelink Ocean

234   Data Assimilation System (BODAS, Oke et al. 2008). The BRAN output data is daily-

235   averaged and is here time-interpolated to be 6 hourly to fit with the atmospheric initial

236   conditions. In an Australian-centred region (75° S - 16° N, 90° E - 180° E) the BRAN data

237   has a resolution of 0.1 degrees, and the WRF model domains used here are within this region.

238   The BRAN data contains complex SST structures in the EAC with mesoscale filaments and

239   eddies present, as can be seen in Figure 4a and d.

240   For the 2012 cases the Bluelink Ocean Model, Analysis and Prediction System

241   (OceanMAPS) version 2 (Brassington et al. 2012) SST is used. As with BRAN, OceanMAPS

242   uses a global ocean model based on the Modular Ocean Model version 4 (MOM4) with

243   assimilated BODAS observations and has a spatial resolution of 0.1 degrees. Since both the

244   BRAN and the OceanMAPS both utilize MOM, they produce qualitatively similar SST

245   structures in the EAC with mesoscale filaments and eddies present, as can be seen in the left

246   column of Figure 4.

247   **Lightning and MCAPE analysis**

248   In addition to the WRF simulations, lightning data from the commercial provider

249   Global Positioning and Tracking System Pty. Ltd. (GPATS 2013) is used to analyse the

250   distribution of thunderstorms in relation to the SST. GPATS data requires the arrival time of

251   a lightning discharge to be recorded at three or more radio receivers (Cummins and Murphy

252   2009). This allows for the detection of return strokes and the ability to distinguish between

253   cloud-to-cloud and cloud-to-ground lightning. The analysis conducted here concentrates on

254   lightning strike locations over given time periods that are compared with the model results

255   over the same periods.

256   The maximum convective available potential energy (MCAPE) is used to investigate

257   the sensitivity of tropospheric vertical instability to the SST distribution. MCAPE is

258   calculated as the CAPE at the level of greatest instability (Colman 1990). Specifically, in the

259   post-processing phase of WRF the MCAPE is calculated as the CAPE from the air parcel

260   with the maximum equivalent potential temperature in the lowest 3 km. CAPE (Moncrieff

261   and Miller 1976) is calculated by integrating the local buoyancy of a parcel from the level of

262   free convection to the equilibrium level. CAPE is a measure of instability through the depth

263   of the troposphere, is related to updraft strength, and is used to indicate thunderstorm

264   potential. MCAPE has been chosen rather than CAPE calculated using a parcel from the

265   surface, to compare with the observed lightning strikes, because the thunderstorms of interest

266   here could be surface based or elevated. Over the strong SST gradients present during these

267   cases the flow of warm moist air over cooler SSTs may lead to the warm air overrunning the

11

268   cooler near-surface air. In these situations it is more insightful to analyse the MCAPE rather

269   than surface based CAPE because the most unstable layer that triggers the thunderstorms may

270   not be at the surface.

271   3. Results

272   For the four ECL case studies the first 12 hours of the 60-hour simulations are not analysed

273   as this is considered a spin up period, which leaves the remaining 48 hours as the analysis

274   period. In the following analysis references to 'detailed run' refer to the BRAN or

275   OceanMAPS SST initialised simulations for the 2007 and 2012 cases respectively. Three

276   different timescales are investigated. The first is the 48-hour average that provides a less

277   noisy signal with which we can identify associations with SST more clearly. Secondly, 12-

278   hour averages provide a view during the different phases of the ECLs' development. Thirdly,

279   for specific lightning active periods, 3-hourly averages allow a view on a timescale more

280   relevant to the thunderstorm lifecycles.

281   2-day average structures

282   The 48-hour average simulated MCAPE for each of the cases is plotted in Figure 5 to

283   provide a general overview of the convective energy situation. The broad distribution of

284   average MCAPE shows some similarities between the detailed and skin SST runs while local

285   differences can be seen. This suggests that the changes to the SST do not lead to large

286   changes in the broad synoptic-scale features of the storms so, for example, the areas of low-

287   level warm advection remain in similar locations and are generally associated with the high

288   MCAPE regions in Figure 5. Also of note is the lack of MCAPE over the land interior with

289   significant MCAPE only occurring over the coastal regions. During the 48-hour period over

290   which these averages are taken there are considerable changes to the MCAPE due to the

291   approach and passage of the cold-core upper-level trough.

In Figure 5 the SSTs are overlaid as black contours (also see Figure 4) to aid visualization of relationships with MCAPE. Comparing Figure 5a and b it is apparent that the warm SSTs over the central warm eddy (centred at 32.5° S, 154.5° E) in JUN07a_BN are responsible for higher 48-hour averaged MCAPE than in JUN07a_skin. Also lower MCAPE in JUN07a_BN located east of the warm eddy over the tongue of cold water near 32° S, 157° E, is largely absent from JUN07a_skin. Of potential significance for the coastal impacts of this case is the MCAPE local maximum of 350 J kg^{-1} seen offshore at 33° S, 153° E that is not present in JUN07a_skin. The JUN07a_BN average 10-metre wind vectors shown in Figure 5a indicate that downwind of this maximum is a large negative temperature gradient associated with cooler water nearer the coast near 33° S, 152.5° E.

For the JUN07b cases (Figure 5c and d) the 48-hour average MCAPE is greater than the JUN07a cases along a broad band oriented southwest to northeast across domain 2. This band of MCAPE is narrower in JUN07b_BN with a sharper southward reduction located near 34° S, 154° E. This occurs in a region of strong SST gradients (cooling southward) along the southern edge of the central warm eddy. Around 31° S, 157.5° E is a region that has the highest averaged MCAPE in JUN07b_BN of either of the JUN07b cases, locally in excess of 600 J kg^{-1}.

For APR12 (Figure 5e and f) there is a broad band of high MCAPE in both cases east of 152° E. APR12_skin has substantially larger, in both magnitude and areal extent, MCAPE within the band, particularly in the southern portions. APR12_skin fails to resolve multiple regions of SST gradients within the southern region that are present in APR12_OM. For the JUN12 cases (Figure 5g and h) there are less prominent MCAPE changes with broadly similar distributions in both JUN12_OM and JUN12_skin. Of note is an area of higher MCAPE in JUN12_OM near 35° S, 156.5° E and lower MCAPE in the region near 37.5° S, 152° E associated with a greater east-west SST drop in JUN12_OM.

317   To further explore the features seen in Figure 5, the 48-hour MCAPE differences

318   between the detailed SST and the skin SST runs are plotted for each case in Figure 6. In this

319   figure positive MCAPE differences are coloured in blue and green because of the association

320   of high MCAPE with heavy rain. The two 2007 cases (Figure 6a and b) show that average

321   MCAPE was greater by between $50 - 100$ J kg^{-1} over the same prominent central warm eddy

322   that persisted through the period covered by the two cases. There is also reduced MCAPE

323   associated with cooler waters in the detailed cases, with the largest reductions east of the

324   central warm eddy in both cases. In JUN07b MCAPE is reduced more than in JUN07a to the

325   east and south of the warm eddy. This corresponds to a larger (cooler) difference in SST in

326   JUN07b in these regions (Figure 4f).

327   The 48-hour-averaged winds for JUN07a_BN in Figure 6a show that the largest

328   positive MCAPE differences occur on the downwind (southern) side of the central warm

329   eddy, with maxima at 33.5° S, 155.5° E and at 33° S, 153° E, the latter location associated

330   with the offshore MCAPE max highlighted in the analysis of Figure 5a. The largest negative

331   MCAPE differences occur on the downwind side of the colder SSTs east of the warm eddy,

332   for example at 33° S, 157° E. In the persistent and strong east-southeasterly flow south of the

333   warm eddy the relationship is less clear, probably due to the strong advection of low-level

334   heat and moisture. Where heat and moisture is advected, regions of elevated MCAPE can be

335   correspondingly displaced. An example of the displacement is found in a region of positive

336   MCAPE difference near 35° S, 155.5° E that is associated with the upstream warm eddy at

337   36° S, 156.5° E. While there are considerable changes to the storm over this 48-hour period,

338   the quasi-stationary nature of the low pressure caused flow to be persistently east-

339   southeasterly across this region, lending confidence to this proposed advection relationship.

340   The JUN07b case provides an interesting comparison with JUN07a because the SST

341   distribution is similar to JUN07a. The average 10-metre wind flow is different to JUN07a and

the MCAPE difference distribution appears correspondingly shifted in Figure 6b. The shift

occurs because the locations of greatest low-level heat and moisture advection off the eddy

are changed because of the different pattern of wind flow. In particular the largest positive

MCAPE differences now occur over the northwest section of the central warm eddy around

32° S, 155° E. The wind vectors indicate that the flow turns from east-south-easterly to

southerly over the warm eddy which means that the region of largest positive MCAPE

difference over the eddy is again over the downwind side. The largest negative MCAPE

differences can also be seen to occur on the downstream side of the regions of cooler SSTs.

The 48-hour CAPE differences associated with the 2012 cases (Figure 6c and d) also

exhibit positive/negative relationships with positive/negative SST difference. The

APR12_OM case contained a warm current jet that spread southward from the southeast

corner of Australia into a warm eddy near 40° S, 151° E as shown in Figure 4g. Cooler water

located east of this feature leads to an east-west dipole in SST that is not present in the

APR12_skin case. Figure 6c shows that these SST features lead to a corresponding east-west

dipole in the MCAPE differences in the region south of 35° S and between 150° and 156° E

and strongest near 40° S, 153° E. The negative MCAPE differences dominate because of the

larger region of negative SST difference. As with the 2007 cases, 48-hour average winds in

APR12_OM show that the greatest negative MCAPE differences occur downwind of the

greatest negative SST differences throughout the central region where average winds are 10

m s^{-1} or more. South of 39° S and east of 153° E, where the average winds are lighter, there is

less downwind displacement of MCAPE consistent with less average lower tropospheric heat

and moisture advection in this region. The region of maximum positive MCAPE difference at

40.5° S, 153° E is less easy to explain. It lies on the eastern edge of the warm eddy in

southerly flow. Potentially, moisture convergence in APR12_OM simulations associated with

the SST gradients in this region (Figure 4g) during the intensification phase of the ECL that

15

367   occurred over this area played a role. Whatever the process, it will be shown later that this

368   region was associated with concentrated thunderstorm activity.

369   Similar correlations occur for the JUN12 case (Figure 6d) between MCAPE

370   difference and SST differences, with MCAPE differences on the downwind sides of SST

371   differences particularly evident in the strong 48-hour average flow south of 38° S. The largest

372   positive MCAPE differences of over 140 J kg^{-1} occur in south-westerly flow over a strong

373   SST gradient region in JUN12_OM on the southeast edge of a warm eddy near 35.5° S, 153°

374   E. There are similar characteristics in the area of largest positive MCAPE difference in

375   APR12 where the maximum is also on the side of the eddy to the right of the wind direction.

376   To investigate whether the observed distribution of thunderstorms shows a

377   relationship with the MCAPE differences, and hence with the SST differences, all GPATS

378   detected lightning strike locations in the domain 2 region for the entire 48-hour analysis

379   periods of each of the four cases are plotted in Figure 7. In the JUN07a case (Figure 7a) a

380   concentration of lightning can be seen over, and south of, the warm eddy with a particularly

381   pronounced area of strikes over the coast in the Newcastle region near 33° S, 152° E.

382   Comparing with the 48-hour total MCAPE differences in Figure 8, the patches of intense

383   lightning over the southern flank of the central warm eddy occur in a region of generally

384   enhanced MCAPE in JUN07a_BN, however the intense lightning plume near the coast is

385   associated with a localized region of suppressed MCAPE (these regions are almost obscured

386   by lightning 'dots' in the Figure, but can be more easily seen in Figure 6a). There is limited

387   lightning over the cooler waters east of the eddy but significant lightning does occur over the

388   cooler water to the south of the warm eddy. Despite the cooler temperatures there is positive

389   MCAPE difference throughout most of this region. The strong south-eastward flow through

390   this region and consequent displaced MCAPE differences point at a potential relationship

391   between the lightning centred at 34.5° S, 154.5° E and the smaller warm eddy at 35.5° S,

392 156.5° E . The plume of lightning strikes that reaches the coast around 33° S is associated

393 with the severe and localized weather impacts that this region near Newcastle experienced.

394 This region lies downwind of the largest positive MCAPE differences identified earlier along

395 the southern edge of the warm eddy. Not all regions of increased MCAPE are associated with

396 lightning strikes. An example is the small region at 34° S, 159° E, which has increased

397 MCAPE but there is no lightning. The relationship between MCAPE and lightning is

398 dependent on many other factors including the presence of a trigger for initializing

399 convection. In this region it is probable that either no trigger was present, or the large-scale

400 forcing was not favourable.

401   For the JUN07b case the lightning occurs over the southeast of the warm eddy with a

402 separate area between 31° and 33° S in the vicinity of 158° E (Figure 7b). These areas are

403 generally associated with the edges of positive MCAPE differences, however the average

404 wind flow is blowing from negative to positive MCAPE difference, which is inconsistent

405 with the hypothesis of along flow SST forcing MCAPE release. Figure 5c showed that this

406 case had substantially higher average MCAPE than JUN07a, potentially leading to more

407 rapid thunderstorm development. In this case the vast majority of lightning was

408 predominantly in the first 24 hours of the period, which will be investigated in greater detail

409 in a following section.

410   The most concentrated region of 48-hour lightning in APR12 (Figure 7c) is in an arc

411 centred around 39.5° S, 152° E. Comparing with the MCAPE differences (Figure 6c) this

412 region can be seen as occurring downstream of the largest MCAPE increases in APR12_OM.

413 A significant amount of lightning occurs over the large region of negative MCAPE

414 differences located south of 36° S, and between 152° and 156° E but most of this region is

415 downwind of MCAPE reductions. Bands and complexes of thunderstorms associated with

416 storm rainbands lead to a complicated picture. In contrast to JUN07a, this case shows a less

417   clear relationship between the lightning and the MCAPE differences. The JUN12 case

418   (Figure 7d) had far less lightning than the other cases and the MCAPE differences do not

419   indicate a clear relationship with the SST.

420   **12 hour snapshots**

421   The focus now turns to investigate the JUN07a case over shorter periods to establish

422   whether SST-induced MCAPE differences and lightning distributions show relationships at

423   timescales closer to those of relevance to different phases of ECL evolution. As the upper

424   level trough moves eastward the instability of the atmosphere generally increases because of

425   the cooling of the upper troposphere. This is one reason why it is important to investigate the

426   MCAPE sensitivity at shorter time-scales. The MCAPE differences (BRAN – Skin) for the

427   four 12-hour periods that make up the 48-hour analysis period are plotted in Figure 9 and the

428   12-hour lightning strike locations in Figure 10. It should be noted that an analysis of coastal

429   rain gauge observations in Chambers et al. (2014) indicates that the simulated heaviest

430   rainfall occurred roughly 6 hours prior to the observed rainfall. This is an indication that the

431   rainband moved southward earlier in the model that in reality.

432   For the first 12-hour period (Figure 9a) it is apparent that MCAPE is higher over and

433   west of the warm eddy in JUN07a_BN. Figure 10a shows a small area of lightning just west

434   of the core of the warm eddy during this period at 32° S, 154.5° E. In the second 12-hour

435   period the largest MCAPE differences occur along the southern flank of the warm eddy with

436   increases of over 400 J kg^{-1} (Figure 9b). This occurs in a region broadly consistent with the

437   concentrated lightning during this period. The area of greatest MCAPE increase occurs

438   slightly south of the lightning, consistent with a more southward location of the rainband by

439   this time.

440   In the third time period, lightning data in Figure 10c show a plume of lightning

441   propagating towards the coast and originating over the region of strong SST gradients. The

442   region of elevated CAPE has propagated further south (Figure 9c). A large region of lowered

443   CAPE, that originates over the cooler water to the east of the warm eddy and is evident at all

444   of the time periods, is most pronounced in the third period. By the fourth time period the

445   CAPE over the warm eddy appears to have recovered somewhat while the southward

446   propagating elevated region has spread further south.

447   As mentioned earlier, the JUN07a simulations had a 6 hour discrepancy in the timing

448   of peak coastal rainfall. In an attempt to take account of this, an additional 12-hour MCAPE

449   difference plot is in Figure 11, where the 12-hour periods for calculating the MCAPE are 6

450   hours earlier than the lightning periods. This plot shows a more clear consistency between the

451   location of increased MCAPE and of lightning strikes associated with a more accurate

452   location of the principal rainband. In particular Figure 11c shows that the plume of

453   thunderstorms that impacted the coast so severely occur in a narrow band of increased

454   MCAPE. The relationship is complicated by the fact that the occurrence of thunderstorms

455   releases CAPE and so if enough storms occur then the MCAPE will decrease. These results

456   show that at a 12-hourly timescale, and accounting for the 6 hour discrepancy with

457   observations, the effect of introducing eddy resolving SSTs is to increase CAPE in regions

458   generally associated with regions of observed thunderstorms.

459   **3-hour analysis**

460   To continue the shift down to smaller timescales, an analysis of the 3-hourly lightning

461   strikes and MCAPE difference over the period over which significant coastal impact occurred

462   (1800 UTC 7 June to 0600 UTC 8 June) has been conducted. 3-hourly timescales are more

463   representative of a thunderstorm complex lifecycle and so are used to look at the instability

464   sensitivity for specific periods of intense thunderstorm activity. At these timescales it is

465   essential to take account of the 6 hour error in the timing of simulated heaviest coastal

466   rainfall. Therefore the MCAPE difference plots are made for 3-hourly periods that starts 6

467   hours earlier than the beginning of each 3-hour lightning period. A potential source of error in

468   this type of analysis could come because of changes to the MCAPE due to the diurnal cycle,

469   however diurnal radiative forcing should be less significant over this region at this time of

470   year (winter). The results of this analysis for four 3-hour periods is shown in Figure 12. For

471   the first two periods (Figure 12a and b) an area of strongly enhanced MCAPE in JUN07a_BN

472   (up to and over 400 J kg^{-1}) can be seen to be propagating southward (with embedded

473   westward propagating regions). Associated with the southern and western sides of this region

474   are areas of concentrated lightning. Figure 12c shows that the lightning extended westward in

475   a plume from the middle of the three lightning patches in the prior 3-hour period. By

476   comparing Figure 12b and c the intense lightning plume can be seen to develop downwind of

477   the area of greatest enhanced MCAPE located along 33° S between 153° and 156° E. In the

478   final 3-hour period the intense lightning continues in this plume and is associated with

479   elevated coastal and upwind MCAPE while regions of suppressed MCAPE occur to the north

480   and south. Figure 12d shows that the largest MCAPE increases over land of the four periods

481   occur in the final period near 33° S, 152° E.

482   **4. Discussion**

483   This research compares lightning data with model MCAPE differences caused by changing

484   the SST input data in an investigation into potential relationships between complex SST

485   structures in the EAC and thunderstorms during ECLs. This was motivated initially by

486   comparisons made between the distribution of lightning and the distribution of SST (for

487   example Figure 7) that suggested a connection between the two. It is also physically

488   motivated since, prior to significant vertical mixing of air, an air mass moving over water

489   would be expected to become more unstable more quickly if SSTs are warmer because

490   warmer waters imply greater surface fluxes of heat and moisture into the boundary layer.

491 Hypothetically the instability should continue to increase unless the low-level air mixes

492 upward and warms the middle and upper layers of the troposphere or if the low-level air

493 reaches thermal and moist near-equilibrium with the ocean surface that prevents further

494 increases in near-surface moist static energy. On the 48-hour average MCAPE differences in

495 Figure 6, there is evidence of this process emerging with MCAPE tending to be larger on the

496 downwind side of areas of warmer waters in the detailed SST runs. However there are a

497 number of other complicating factors to consider with respect to this process, three of which

498 we discuss below.

499   The first complication comes from the effect changes in SST can have on the surface

500 wind speed. Past research (see review by Small et al 2008) suggests that surface winds tend

501 to increase over warm water because greater vertical thermal instability mixes momentum

502 from aloft down to the surface. If this is assumed to be the case then this effect will change

503 the vertical wind shear profile which is known to be important for thunderstorm development

504 and severity. There is a further surface wind complication that is not generally considered in

505 the previous research which concerns situations where the momentum aloft is weaker than, or

506 opposing, the surface flow. In these situations the vertical mixing of momentum over warmer

507 waters should decrease the surface winds, not increase them, with consequent vertical wind

508 shear changes.

509   A second complication issue is associated with the formation of the thunderstorms

510 themselves. In a classic thunderstorm situation the thunderstorm will be triggered once

511 warming and moistening of the boundary layer is enough for a lifted parcel to overcome

512 convective inhibition. Once the thunderstorm occurs it will tend to warm the middle and

513 upper troposphere and consequently reduce the CAPE. It is therefore not difficult to imagine

514 situations where warmer water areas are associated with reduced CAPE caused by areas of

515 moist convection triggered by the same, or other areas of warmer waters.

The third complication comes from the impact of SST on the broader storm due to processes such as baroclinic instability. The APR12 case stands out as the most prominent example of the four cases that exhibited complications of this kind. In this case the storm was more compact and intense in APR12_OM than in APR12_skin and this impacted the distributions of MCAPE differences substantially, particularly in the later hours of the simulations.

With these considerations in mind the lightning data analysis reveals a complicated but at times marked relationship between eddy and filament structures in the EAC. On the 48-hour timescale, increased MCAPE shows a clear relationship with increased SST with displacement of MCAPE difference from SST difference occurring in regions consistent with low level heat and moisture advection. The effect of the complex SST patterns is to rearrange the pattern of MCAPE across the region and we hypothesize that this process also re-arranges the distribution of thunderstorms. Further evidence for this hypothesis is found when shorter timescales, more relevant to thunderstorm processes, are considered. The 3-hourly analysis of the JUN07a case during the period of greatest coastal impact shows that regions of elevated MCAPE associated with changing the SST occur in regions consistent with lightning activity. On these shorter timescales increased MCAPE associated with changing the SST shows less of a correlation with SST differences.

The 3-hourly results emphasize the importance of including accurate SSTs in future numerical forecasts of similar events on this fine scale. The results suggest that the instability in the thunderstorm band was significantly increased because of the warm eddy present offshore. The effect of the eddy and associated SST gradients along its southern flank increase the convectively instability and focus it into a narrow band in a consistent location with respect to the observed thunderstorm band. The significant damaging impacts were largely associated with this focussed thunderstorm band despite the fact that the low pressure

541   system covered a much broader region. Since the model results suggest this region may be

542   more favourable for thunderstorms in the BRAN simulations through increased MCAPE, it is

543   evidence that this highly significant storm feature was directly triggered by the warm eddy

544   and associated strong SST gradient.

545   Past research on the effect of SST gradients on surface winds has shown that

546   convergence tends to occur when air flows from a warm to a cold sea surface (e.g. Sweet et

547   al. 1981). Given this relationship, the maximum in MCAPE difference seen on the 48-hour

548   average in JUN07a in Figure 6a along the southern edge of the warm eddy could be explained

549   by a couple of factors. The first is that on the low-level flow trajectory beyond this point (to

550   the south), the MCAPE tends to release because the convergence over the strong SST

551   gradient provides enough uplift to trigger deep convection. This is consistent with Kuwano-

552   Yoshida et al. (2010) who found evidence of deep convection and thunderstorms

553   preferentially occurring over strong SST gradients. Under the northwest average flow over

554   the eddy, the southern edge of the eddy has a tendency to be the final point on the trajectory

555   that built up MCAPE across the warm eddy, and therefore should have the highest MCAPE

556   value. The second influence might be from higher moisture content within a region of

557   moisture convergence forced by the SST gradient. This should increase the dew point

558   temperature that will tend to increase the MCAPE (all other factors remaining equal). This

559   complicated process will require further detailed work and analysis.

560   A warm eddy in JUN12_OM near 35° S, 152° E is associated with the greatest

561   positive MCAPE differences. This region is also where the low pressure intensified and on

562   initial impression it appears that the low tracks along the SST gradient on the edge the eddy

563   (not shown). Despite this impression the JUN12_Skin simulation, that does not resolve an

564   eddy in this location, produced a very similar track and reached a similar intensity to

565   JUN12_BN. This point is made because it suggests that in this case the impression of a track

566 along an SST gradient may not be causal (as suggested by Holland et al. 1987 for a similar

567 case) but coincidental and instead possibly governed by other factors such as synoptic or

568 topographic steering.

569   Overall, a cold pool of air in the middle troposphere associated with ECL

570 development moving over a focussed region of warm water is conducive to vertical

571 instability that will be released where there is a convective trigger. This release happens

572 within broad scale storm triggers such as fronts, rainbands, topography, and as this study

573 suggests, SST features. The four cases studies show that the relationship between SST and

574 thunderstorm development during ECLs is not straightforward, but is compelling. For the

575 most damaging case, the results strongly indicate that the severe thunderstorm rainband was

576 intensified because of the large warm offshore eddy and its associated southern side strong

577 SST gradient.

5. Conclusion

579 The relationship between thunderstorm distributions and SST has been investigated using

580 lightning data and WRF simulations for four ECLs. WRF simulations initialised with coarse

581 SSTs are compared with detailed SST runs. Complex eddy and frontal structures in the

582 detailed SST runs cause MCAPE increases associated with regions of warmer SST and

583 decreases associated with colder SST. There is evidence that horizontal heat and moisture

584 advection displaces the MCAPE changes downwind. At 3 hour timescales, the differences in

585 MCAPE become larger and more localized and show a compelling correlation with the

586 observed lightning. The focused study of the 7-9 June 2007 case has shown that the plume of

587 thunderstorms associated with the coastal damage occurs downwind of the region of

588 enhanced MCAPE on the southern flank of the EAC warm eddy present at the time.

589 It is concluded that the complex upper ocean heat content structure present during this case

590 significantly influenced the impact from thunderstorms. Therefore an accurate eddy resolving

591 SST dataset may be important for accurate forecasts of future storms of similar nature.

592 **Acknowledgments**

1. References

600 Alexander GD Weinman JA Karyampudi VM Olson WS Lee ACL (1999) The effect of

601 assimilating rain rates derived from satellites and lightning on forecasts of the 1993

602 superstorm. Mon Weather Rev 127:1433-1457

603

604 Andrews JC Scully-Power P (1976) The structure of an East Australian Current anticyclonic

605 eddy. J Phys Oceanogr 6:756-765

606

607 Abarca SF Corbosiero KL (2011) The World Wide Lightning Location Network and

608 convective activity in tropical cyclones. Mon Weather Rev 139:175–191

609

610   Betts AK Miller MJ (1986) A new convective adjustment scheme. Part II: Single column

611   tests using GATE wave, BOMEX, and Arctic air-mass data sets. Q J R Meteorol Soc

612   112:693–709

613

614   Black RA Hallett J (1999) Electrification in hurricanes. J Atmos Sci 56:2004–2028

615

616   Brassington GB Summons N Lumpkin R (2011) Observed and simulated Lagrangian and

617   eddy characteristics of the East Australian Current and the Tasman Sea. Deep Sea Res

618   58:559-573

619

620   Brassington GB et al (2012) Ocean Model, Analysis and Prediction System version 2.

621   CAWCR Tech Rep 52 http://www.cawcr.gov.au/publications/technicalreports/CTR_052.pdf.

622   Accessed 13 August 2014

623

624   Bridgman H (1985) The Sygna storm at Newcastle-12 years later. Meteorol Aust 3:10-16

625

626   Browning SA Goodwin ID (2013) Large-scale influences on the evolution of winter

627   subtropical maritime cyclones affecting Australia's east coast. Mon Weather Rev 141:2416-

628   2431

629

630   Buechler DE Christian HJ Goodman SJ (1994) Rainfall estimation using lightning data.

631   Seventh Conf on Satell Meteorol and Oceanogr, Monterey, CA, Amer Meteorol Soc, June 6-

632   10, 171–174

633

634 Cecil DJ Zipser EJ (1999) Relationships between tropical cyclone intensity and satellite-

635 based indicators of inner core convection: 85-GHz ice-scattering signature and lightning.

636 Mon Weather Rev 127:103–123

637

638 Chambers CRS Brassington GB Simmonds I Walsh K (2014) Precipitation changes due to

639 the introduction of eddy-resolved sea surface temperatures into simulations of the "Pasha

640 Bulker" Australian east coast low of June 2007. Meteorol Atmos Phys 125:1-15 doi:

641 10.1007/s00703-014-0318-4

642

643 Chang D-E Weinman JA Morales CA Olson WS (2001) The effect of spaceborne microwave

644 and ground-based continuous lightning measurements on forecasts of the 1998 Groundhog

645 Day storm. Mon Weather Rev 129:1809-1833

646

647 Christian HJ et al (2003) Global frequency and distribution of lightning as observed from

648 space by the Optical Transient Detector. J Geophys Res 108:4005

649

650 Colman BR (1990) Thunderstorms above frontal surfaces in environments without positive

651 CAPE. Part I: A climatology. Mon Weather Rev 118:1103-1121

652

653 Cummins KL Murphy MJ (2009) An overview of lightning locating systems: History,

654 techniques, and data uses, with an in-depth look at U.S. NLDN.IEEE Trans Electromagn

655 Compat 51:499–518

656

657 DeMaria M DeMaria RT Knaff JA Molenar D (2012) Tropical cyclone lightning and rapid

658 intensity change. Mon Weather Rev 140:1828–1842

659

660   Dowdy AJ Mills GA Timbal B Wang Y (2013a) Changes in the risk of extratropical cyclones

661   in eastern Australia. J Clim 26:1403-1417

662

663   Dowdy AJ Mills GA Timbal B (2013b) Large-scale diagnostics of extratropical cyclogenesis

664   in eastern Australia. Int J Climatol 33:2318-2327

665

666   Dudhia J (1989) Numerical study of convection observed during the Winter Monsoon

667   Experiment using a mesoscale two-dimensional model. J Atmos Sci 46:3077–3107

668

669   Evans JL Guishard MP (2009) Atlantic subtropical storms. Part I: Criteria and composite

670   analysis. Mon Weather Rev 137:2065-2080

671

672   Fandry CB Leslie LM (1984) A two-layer quasi-geostrophic model of summer trough

673   formation in the Australian subtropical easterlies. J Atmos Sci 41:807-818

674

675   Global Climate and Weather Modeling Branch (2003) The GFS atmospheric model. NCEP

676   Off Note 442 http://www.emc.ncep.noaa.gov/officenotes/newernotes/on442.pdf. Accessed 13

677   August 2014.

678

679   GPATS (2013) Global Position and Tracking Systems, a revolution in lightning detection and

680   warning technology. http://www.gpats.com.au. Accessed 13 August 2014

681

682   Griffies SM Harrison MJ Pacanowski RC Rosati A (2004) A technical guide to MOM4.

683   GFDL Ocean Group Tech Rep 5

684

685   Hamon BV (1965) The East Australian Current, 1960-1964. Deep-Sea Res 12:899-921

686

687   Hart RE (2003) A cyclone phase space derived from thermal wind and thermal asymmetry.

688   Mon Weather Rev 131:585-616

689

690   Hobbs PV (1987) The Gulf-Stream rainband. Geophys Res Lett 14:1142–1145

691

692   Holland GJ Lynch AH Leslie LM (1987) Australian east-coast cyclones. Part 1: Synoptic

693   overview and case study. Mon Weather Rev 115:3024-3036.

694

695   Hong S-Y Noh Y Dudhia J (2006) A new vertical diffusion package with an explicit

696   treatment of entrainment processes. Mon Weather Rev 134:2318–2341

697

698   Janjic ZI (1994) The step-mountain eta coordinate model: Further developments of the

699   convection, viscous sublayer, and turbulence closure schemes. Mon Weather Rev 122:927–

700   945

701

702   Kuwano-Yoshida A Minobe S Xie S-P (2010) Precipitation response to the Gulf Stream in an

703   atmospheric GCM. J Clim 23:3676–3698

704

705   Li Y Carbone RE (2012) Excitation of rainfall over the tropical western Pacific.

706   J Atmos Sci 69:2983-2994

707

708   Li X Zheng W Pichel WG Zou C-Z Clemente-Colón P Friedman KS (2004) A cloud line

709   over the Gulf Stream. Geophys Res Lett 31:14

710

711   McInnes KL Leslie L McBride J (1992) Numerical simulation of cut-off lows on the

712   Australian East Coast: Sensitivity to sea-surface temperature. Int J Climatol 12:783-795

713

714   Mills GA Webb R Davidson NE Kepert J Seed A Abbs D (2010) The Pasha Bulker east coast

715   low of 8 June 2007. CAWCR Tech Rep 023

716

717   Minobe S Kuwano-Yoshida A Komori N Xie S-P Small RJ (2008) Influence

718   of the Gulf Stream on the troposphere. Nature 452:206–209

719

720   Miyama T Nonaka M Nakamura H Kuwano-Yoshida A (2012) A striking early-

721   summer event of a convective rainband persistent along the warm Kuroshio in the East China

722   Sea. Tellus A 64:18962

723

724   Mlawer EJ Taubman SJ Brown PD Iacono MJ Clough SA (1997) Radiative transfer for

725   inhomogeneous atmosphere: RRTM, a validated correlated-k model for the longwave. J

726   Geophys Res 102:16663–16682

727

728   Moncrieff MW Miller MJ (1976) The dynamics and simulation of tropical cumulonimbus

729   and squall lines. Q J R Meteorol Soc 120:373–94

730

731   Oke PR Brassington GB Griffin DA Schiller A (2008) The Bluelink ocean data assimilation

732   system (BODAS). Ocean Model 21:46–70

733

734 Orville RE Vonnegut B (1974) Lightning detection from satellites. In: Dolezalek H Reiter R

735 (eds) Electrical processes in atmospheres. Steinkopff Verlag, pp 750–753

736

737 Orville RE Henderson RW Basart LF (1983) An east coast lightning detection network. Bull

738 Am Meteorol Soc 64:1029–1037

739

740 Pepler AS Di Luca A Ji F Alexander LV Evans JP Sherwood SC (2014) Impact of

741 identification method on the inferred characteristics and variability of Australian East Coast

742 Lows. Mon Weather Rev 143:864-877

743

744 Pessi A Businger S (2009) Relationships between lightning, precipitation, and hydrometeor

745 characteristics over the North Pacific Ocean. J Appl Meteorol Climatol 48:833-848

746

747 Qi L Leslie L Speer M (2006) Climatology of cyclones over the southwest Pacific: 1992-

748 2001. Meteorol Atmos Phys 91:201-209

749

750 Rutledge SA Williams ER Keenan TD (1992) The Down Under Doppler and Electricity

751 Experiment (DUNDEE): Overview and preliminary results. Bull Am Meteorol Soc 73:3–16

752

753 Sasaki YN Minobe S Minobe T Asai T Inatsu M (2012) Influence of the Kuroshio in the East

754 China Sea on the early summer (Baiu) rain. J Clim 25:6627–6645

755

756   Schiller A Oke PR Brassington GB Entel M Fiedler R Griffin DA Mansbridge JV (2008)

757   Eddy-resolving ocean circulation in the Asian-Australian region inferred from an ocean

758   reanalysis effort. Prog Oceanogr 76:334-365

759

760   Skamarock WC Klemp JB Dudhia J Gill DO Barker DM Wang W Powers JG (2005) A

761   description of the Advanced Research WRF Version 2. NCAR Tech Note 468

762

763   Small TJ et al (2008) Air–sea interaction over ocean fronts and eddies. Dyn Atmos Oceans

764   45:274–319

765

766   Squires K Businger S (2008) The morphology of eyewall lightning outbreaks in two

767   category-5 hurricanes. Mon Weather Rev 136:1706–1726.

768

769   Stammer D (1997) Global characteristics of ocean variability from regional TOPEX/

770   POSEIDON altimeter measurements. J Phys Oceanogr 27:1743–1769

771

772   Sweet W Fett R Kerling J Violette PL (1981) Air-sea interaction effects in the lower

773   troposphere across the north wall of the Gulf Stream. Mon Weather Rev 109:1042-1052

774

775   Tanimoto Y Kanenari T Tokinaga H Xie S-P (2011) Sea level pressure minimum

776   along the Kuroshio and its extension. J Clim 24:4419–4434

777

778   Thompson G Rasmussen RM Manning K (2004) Explicit forecasts of winter precipitation

779   using an improved bulk microphysics scheme. Part I: Description and sensitivity analysis.

780   Mon Weather Rev 132:519–542

781

782 Trunk TJ Bosart LF (1990) Mean radar echo characteristics during project GALE. Mon

783 Weather Rev 118:459–469

784

785 Vianna ML Menezes VV Pezza AB Simmonds I (2010) Interactions between Hurricane

786 Catarina (2004) and warm core rings in the Southern Atlantic Ocean. J Geophys Res 115:

787 C07002

788

789 Warner TT Lakhtakia MN Doyle JD (1990) Marine atmospheric boundary layer circulations

790 forced by Gulf Stream sea surface temperature gradient. Mon Weather Rev 118:309–323

791

792 Weisman ML Skamarock WC Klemp JB (1997) The resolution dependence of explicitly

793 modeled convective systems. Mon Weather Rev 125:527–548

794

795 Williams ER Rutledge SA Geotis SG Renno N Rasmussen E Rickenbach T (1992) A radar

796 and electrical study of tropical ''hot towers.'' J Atmos Sci 49:1386–1395

797

798 Xu H Xu M Xie S-P Wang Y (2011) Deep Atmospheric Response to the Spring Kuroshio

799 over the East China Sea. J Clim 24:4959–4972.

800

801 **Tables and figures**

802 Table 1: WRF simulation names, dates, and SST data used.

Case name	Dates	SST data input
JUN07a_skin	1200 UTC 6 to 0000 UTC 9 June 2007	NCEP skintemps

JUN07a_BN		BRAN
JUN07b_skin	0000 UTC 15 to 1200 UTC 17 June 2007	NCEP SSTs
JUN07b_BN		BRAN
APR12_skin	1200 UTC 23 to 0000 UTC 26 April 2012	NCEP skintemps
APR12_OM		OceanMAPS
JUN12_skin	0000 UTC 3 to 1200 UTC 5 June 2012	NCEP skintemps
JUN12_OM		OceanMAPS

803
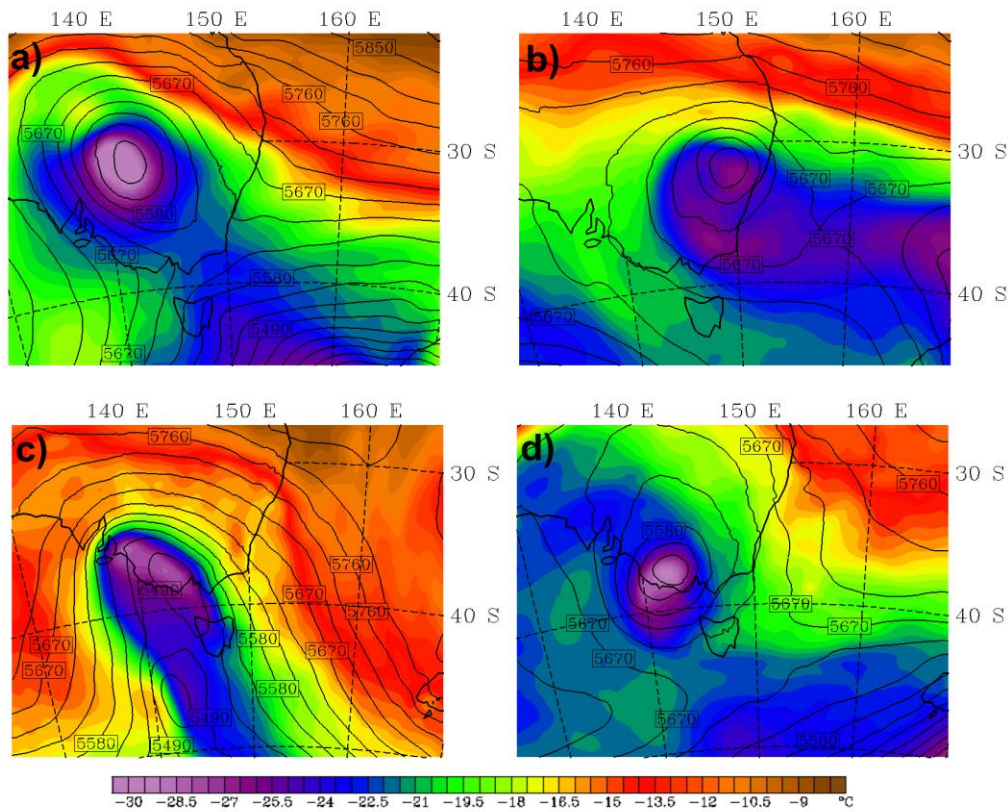
804

Figure 1: Initial domain 1 500 hPa temperatures (°C) and heights (m) for each case; a) 1200

UTC 6 June 2007, b) 0000 UTC 15 June 2007, c) 1200 UTC 23 April 2012, and d) 0000

UTC 3 June 2012.
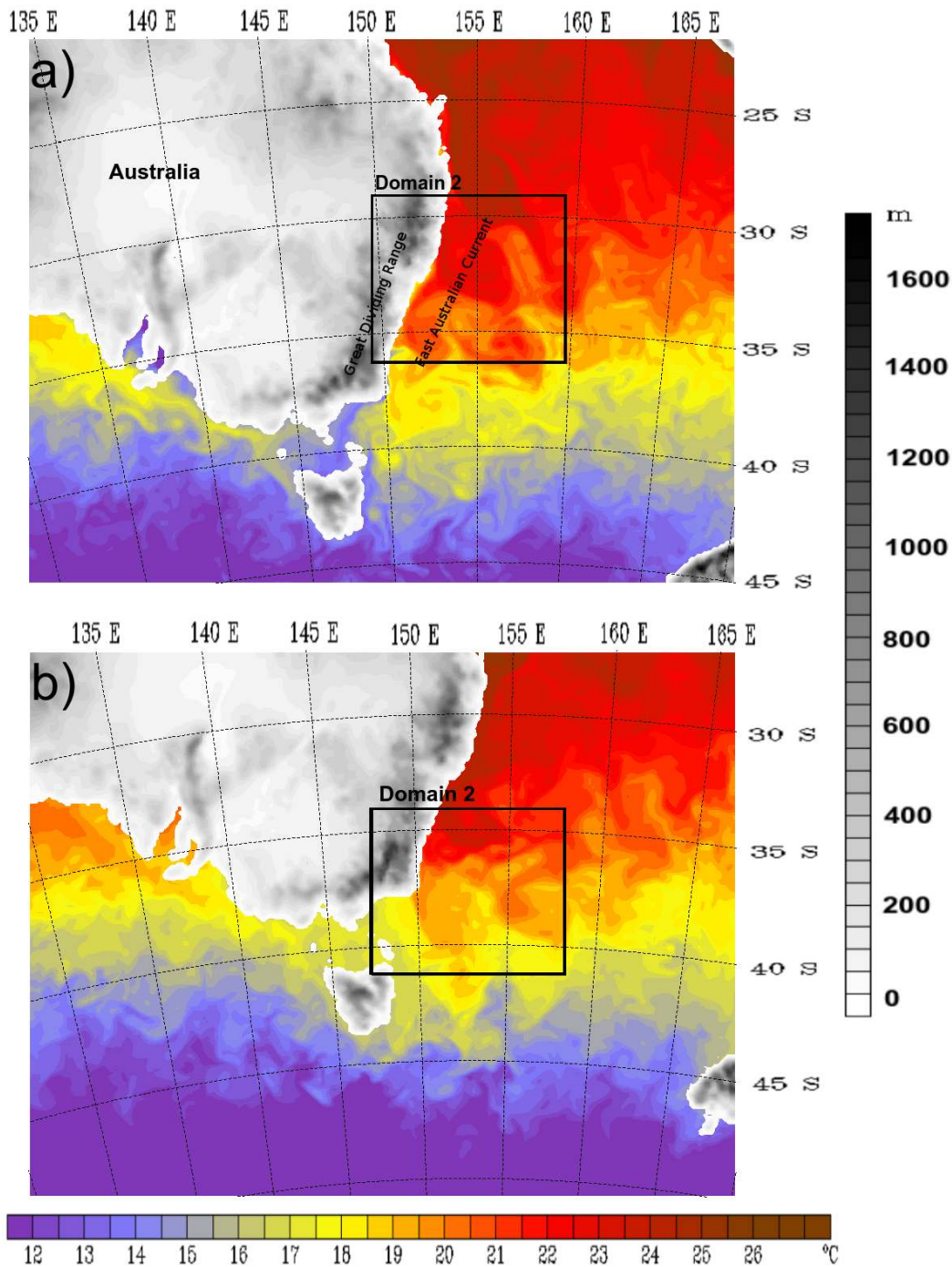
Figure 2: 15 km (whole map) and 3 km (inner box) resolution domains with terrain height (m) for a) the 2007 cases (with BRAN SST for 1200 UTC 6 June 2007 plotted over the ocean), and b) the 2012 cases (with OceanMAPS SST for 1200 UTC 23 April 2012 plotted over the ocean).
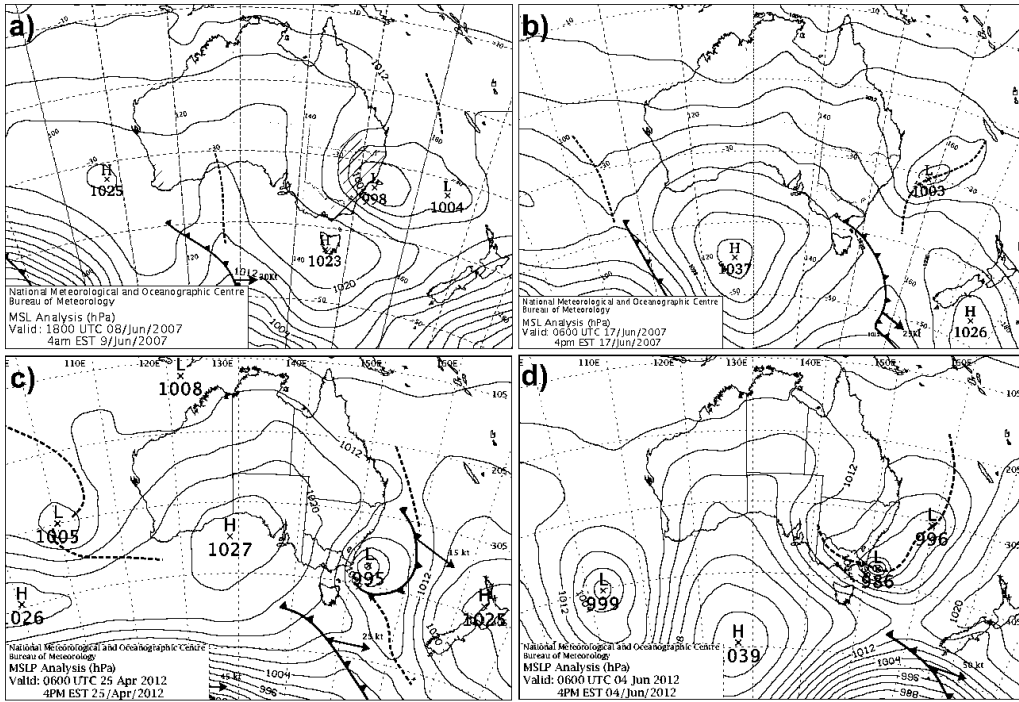
Figure 3: Sea level pressure analyses from the National Meteorological and Oceanographic Centre, Australian Bureau of Meteorology for the time of lowest analysed sea level pressure for each case; a) 1800 UTC 8 June 2007, b) 0600 UTC 17 June 2007, c) 0600 UTC 25 April 2012, and d) 0600 UTC 4 June 2012. Hatched areas indicate rainfall.
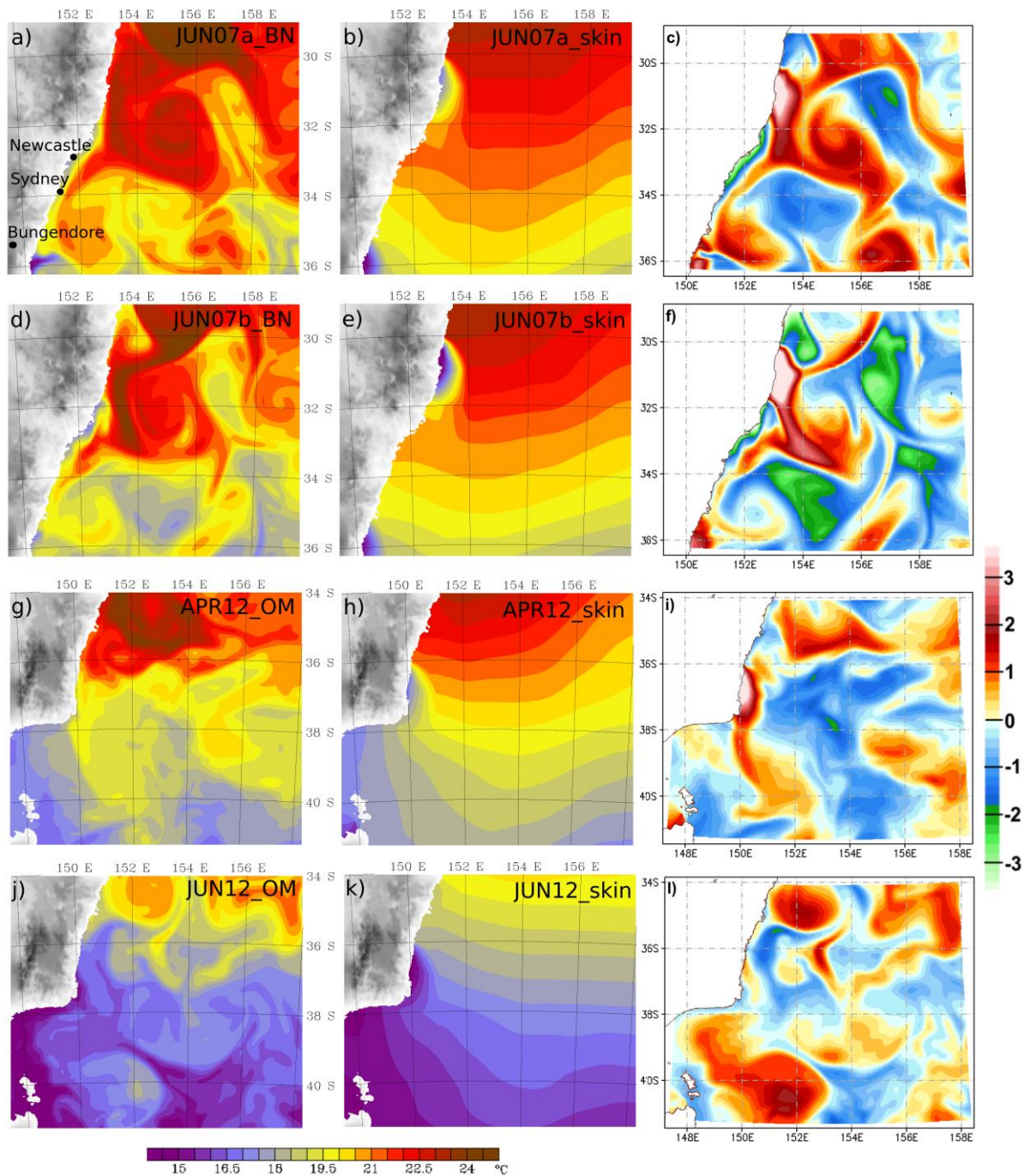
Figure 4: Comparison of initial domain 2 SST inputs into each of the WRF simulations (labelled in top right, refer to Table 1) for 1200 UTC 6 June 2007 [a) and b)], 0000 UTC 15 June 2007 [d) and e)], 1200 UTC 23 April 2012 [g) and h)], and 0000 UTC 3 June 2012 [j) and k)]. In the right column are the 48-hour averaged SST differences (detailed – skin, °C) for the analysis period of each case.
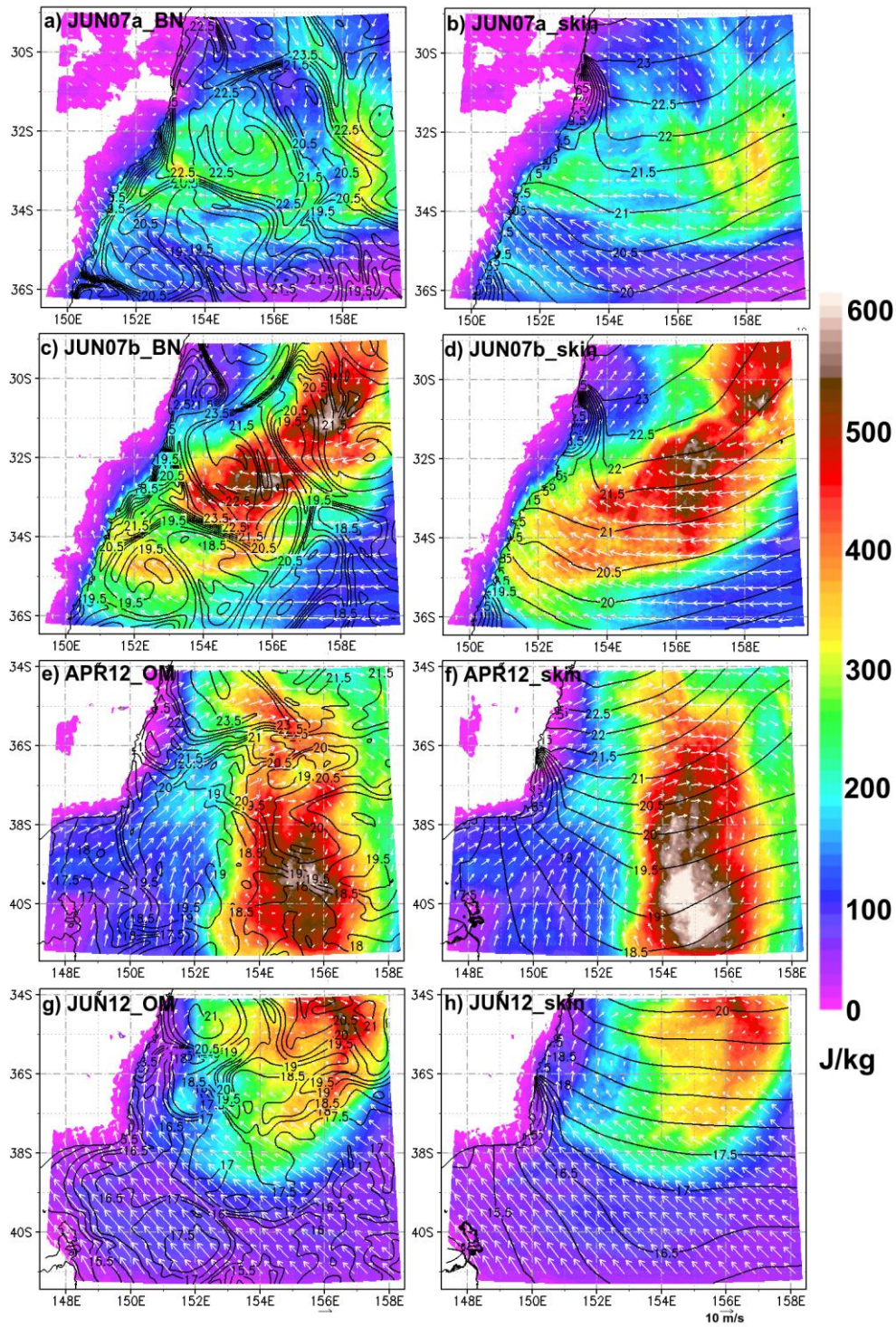
Figure 5: 48-hour averaged MCAPE (J kg^{-1}, colours), SST (°C, black contours), and 10-metre wind vectors (m s^{-1}, representative 10 m s^{-1} vector in bottom right) for the cases as labelled in the top left of each panel.
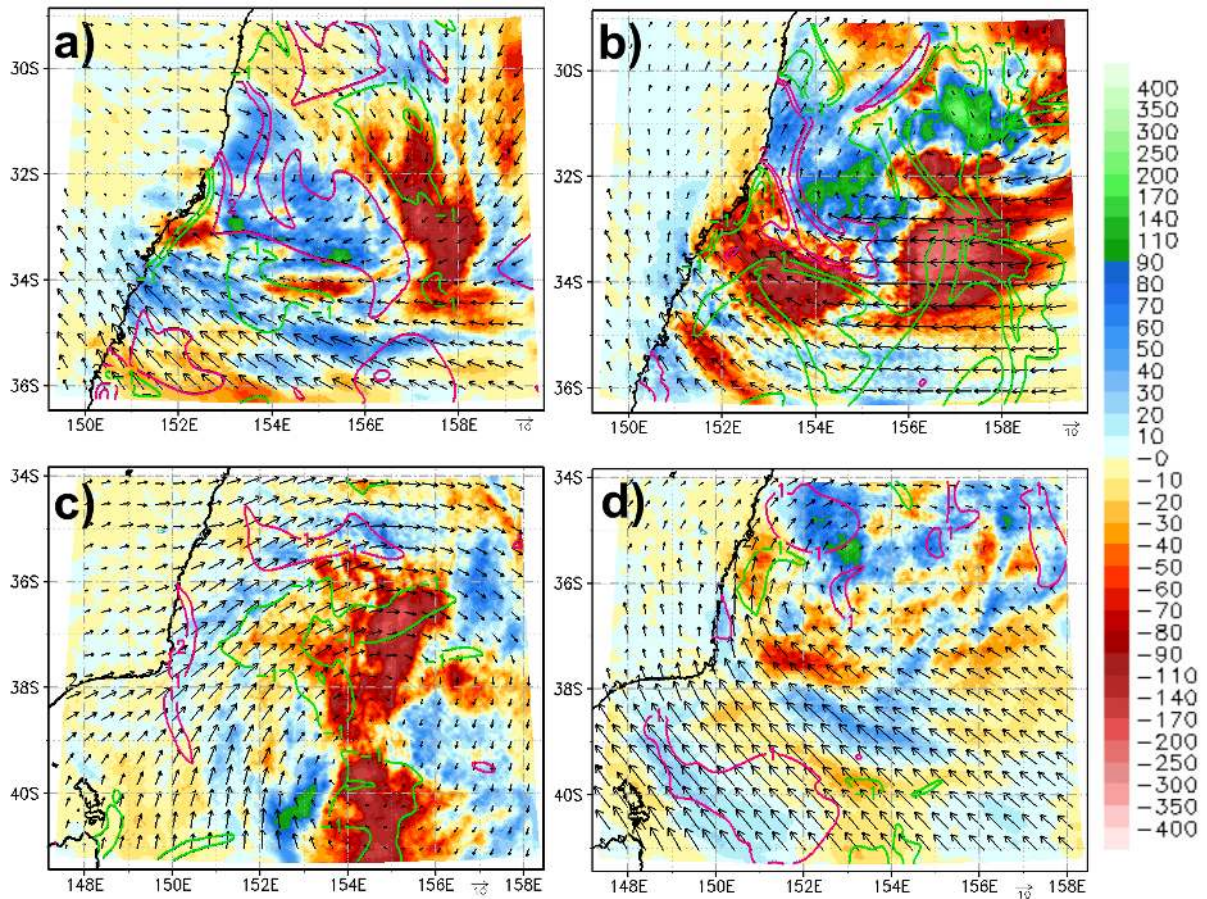
806

Figure 6: 48-hour average MCAPE differences (colours) and SST differences (magenta for +1 and +2 °C and green for -1 and -2 °C) for a) JUN07a_BN – JUN07a_skin b) JUN07b_BN – JUN07b_skin c) APR12_OM – APR12_skin and d) JUN12_OM – JUN12_skin. The 48-hour average 10 metre wind vectors for the detailed runs are overlaid (m s^{-1}, representative vector in bottom right).
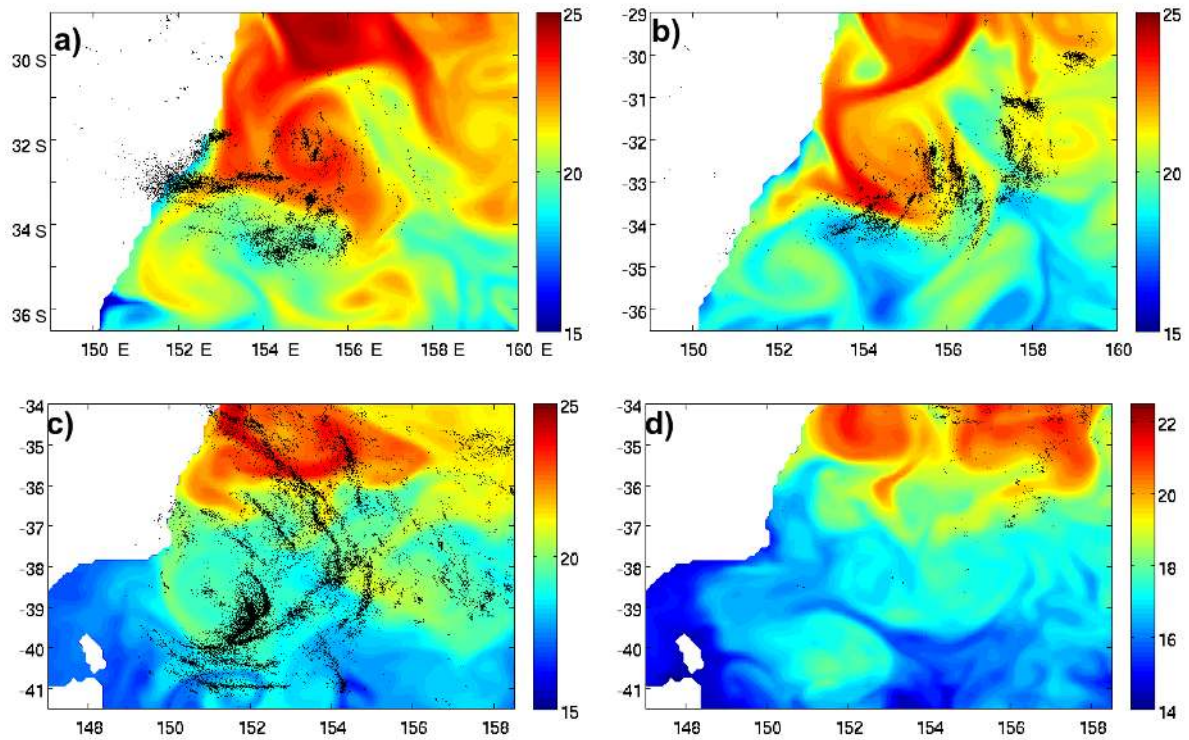
807

Figure 7: 48-hour total detected Global Position and Tracking System (http://www.gpats.com.au) lightning strikes (black dots) for a) 0000 UTC 7 June to 0000 UTC 9 June 2007, b) 1200 UTC 15 June to 1200 UTC 17 June 2007, c) 0000 UTC 24 April to 0000 UTC 26 April 2012, and b) 1200 UTC 3 June to 1200 UTC 5 June 2012. Daily BRAN (for 2007 cases) or OceanMAPS (for 2012 cases) SST is plotted in colour for the initial day in each period.
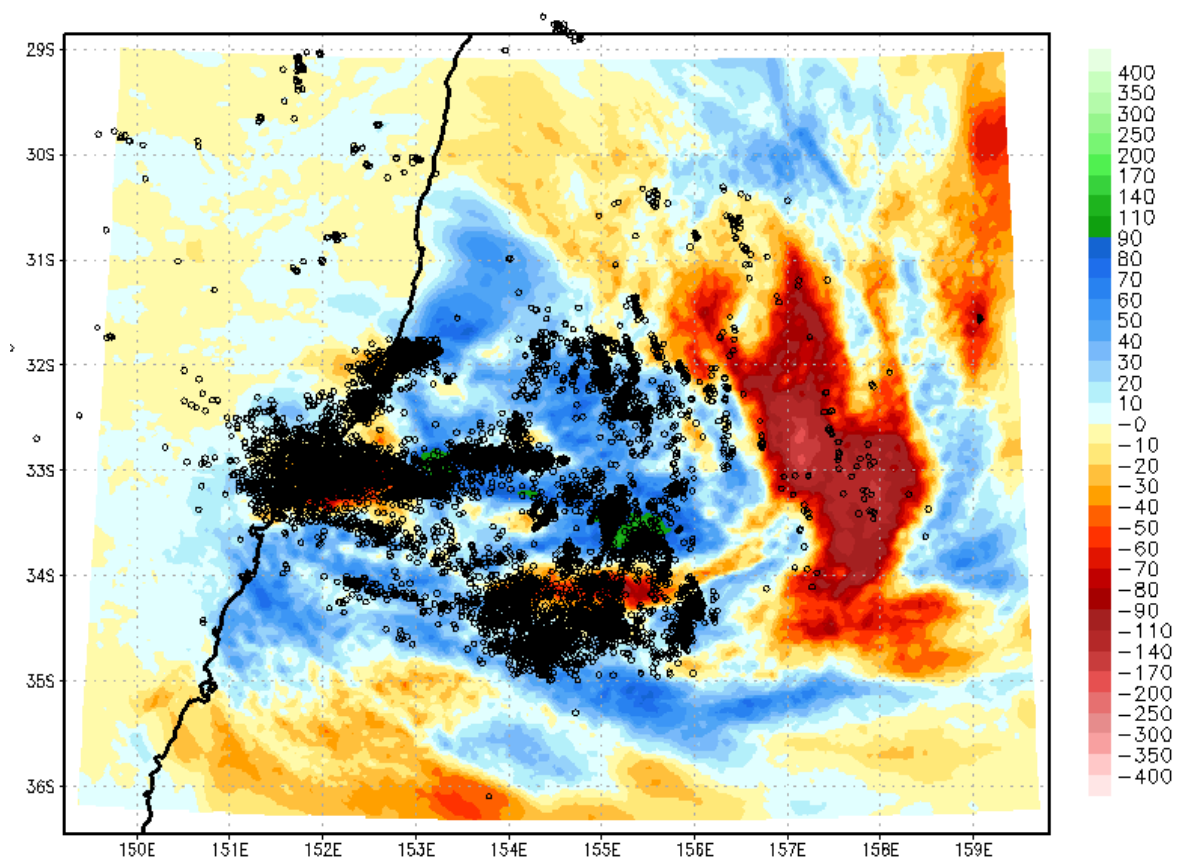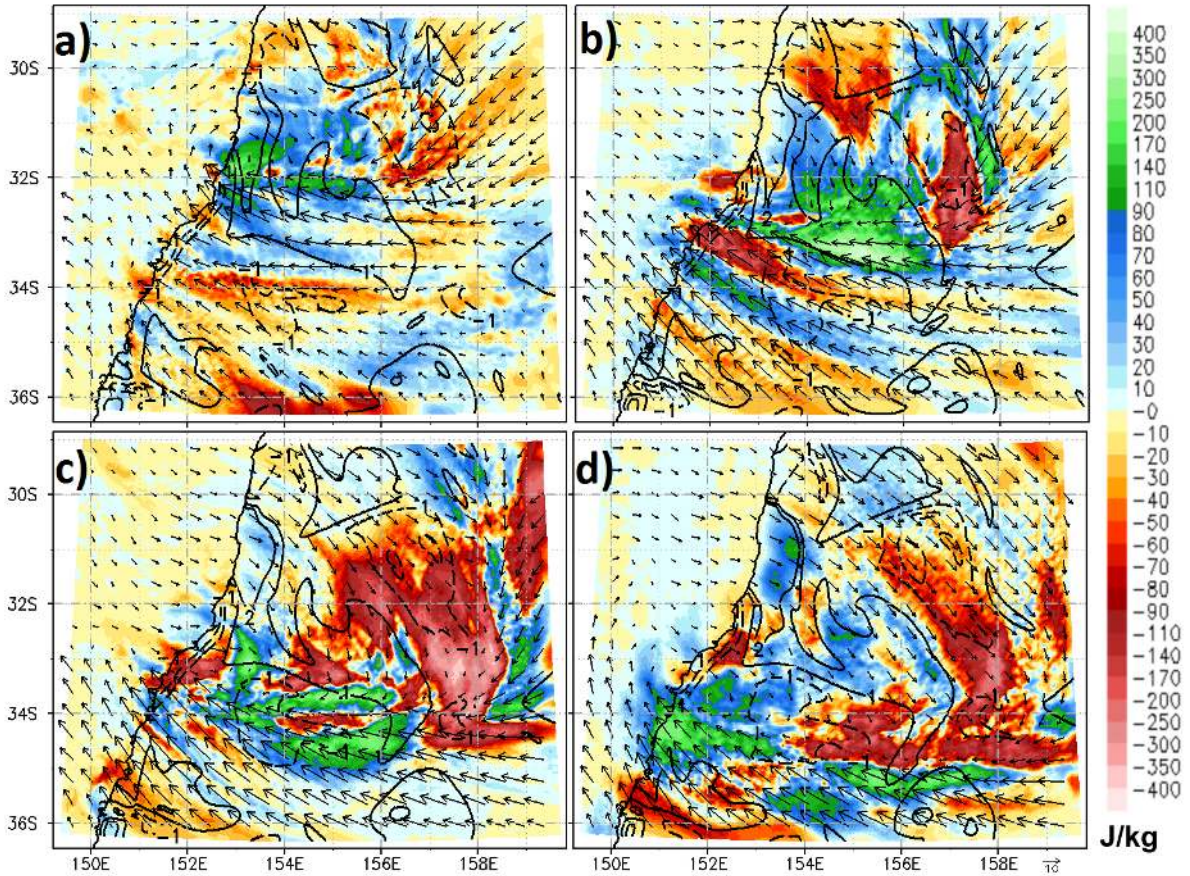
Figure 8: JUN07a 48-hour MCAPE difference (JUN07a_BN – JUN07a_skin, J kg^{-1}) and GPATS observed lightning strike locations (black circles).

808

Figure 9: 12-hourly averaged MCAPE differences (JUN07a_BRAN – JUN07a_skin) for a) 0000 to 1200 UTC 7 June, b) 1200 UTC 7 June to 0000 UTC 8 June, c) 0000 UTC to 1200 UTC 8 June, and d) 1200 UTC 8 June to 0000 UTC 9 June. Corresponding 12-hour averaged SST difference (solid black contours for +1 and +2 °C and dashed for -1 and -2 °C) and JUN07a_BRAN 10 metre wind vectors are overlayed as where dashed contours indicate negative SST difference.
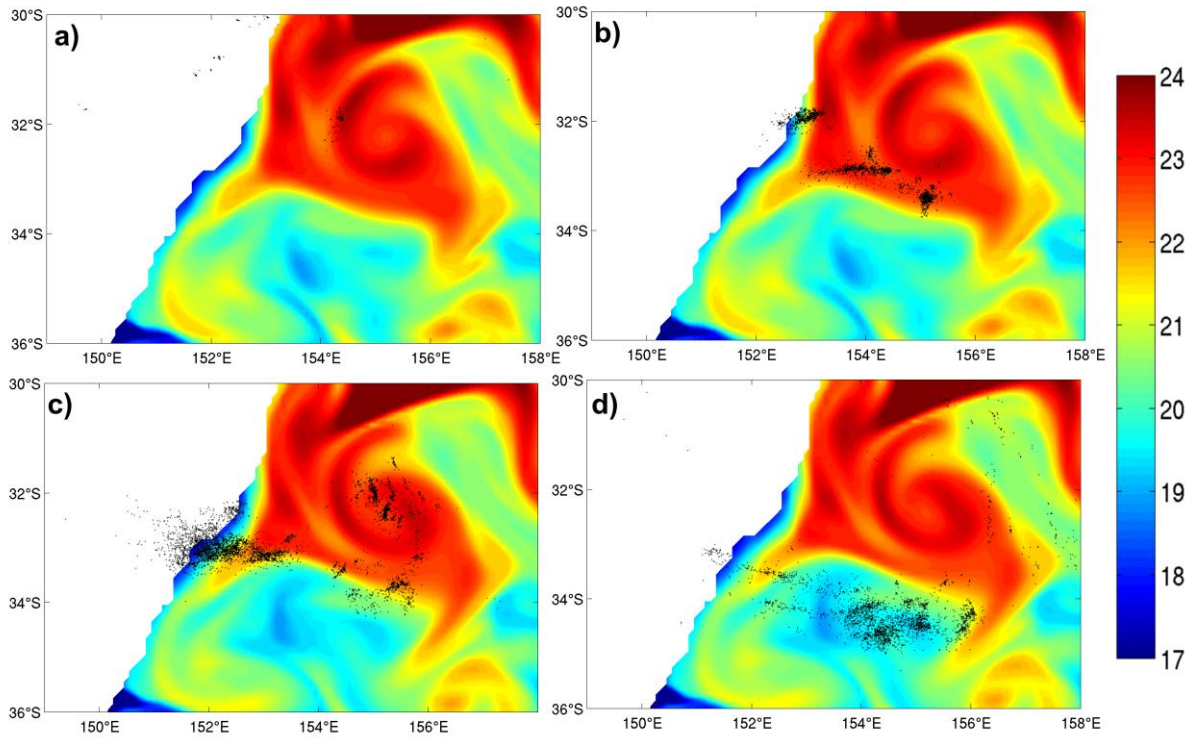
809

Figure 10: 12-hourly GPATS lightning overlaid on BRAN SST (°C, at start time of each period) for a) 0000 to 1200 UTC 7 June, b) 1200 UTC 7 June to 0000 UTC 8 June, c) 0000 UTC to 1200 UTC 8 June, and d) 1200 UTC 8 June to 0000 UTC 9 June.
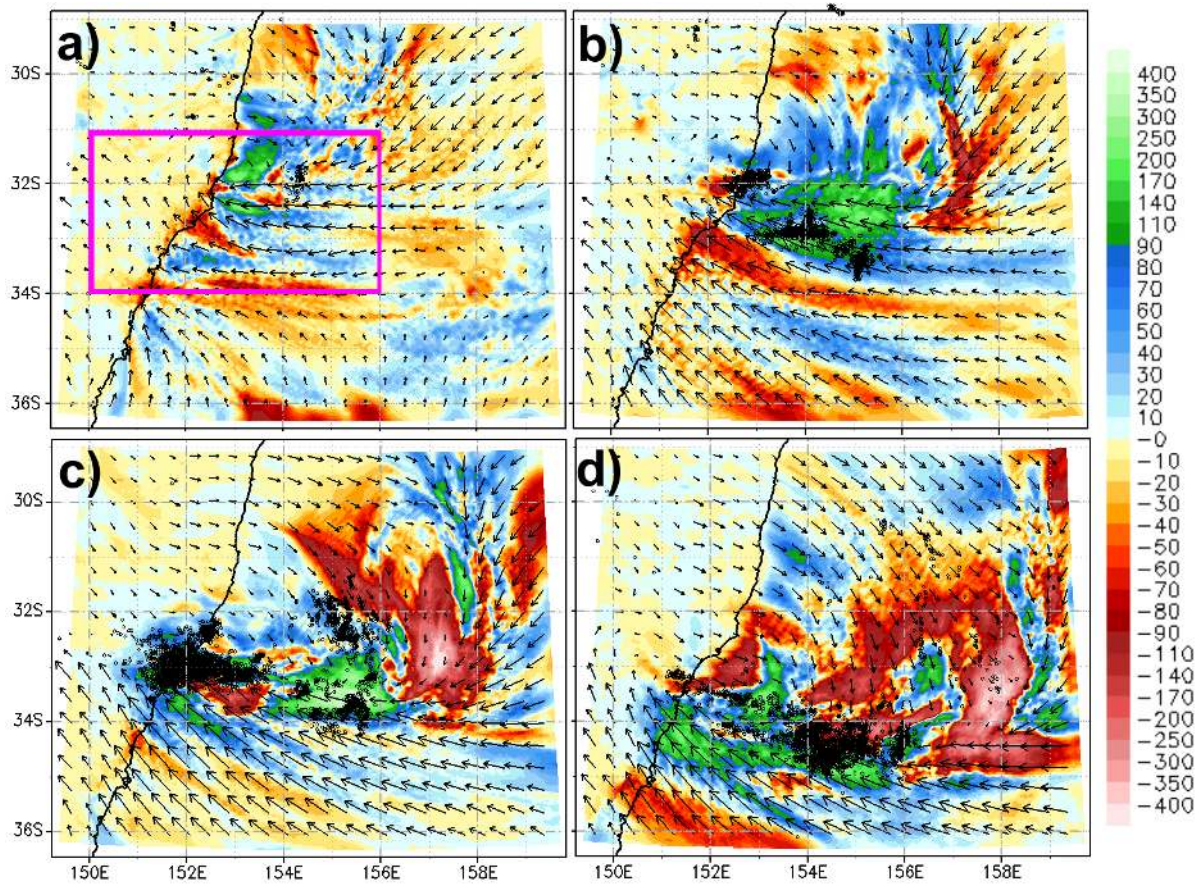
Figure 11: 12-hourly MCAPE difference and winds as in Figure 9 but for 6 hours earlier, plotted to account for the 6 hour lead seen in the model over the observed, rainfall. Overlaid as black dots are the lightning strikes for the original 12-hour periods as defined in Figure 10. The pink box outlines the zoomed region in Figure 12.
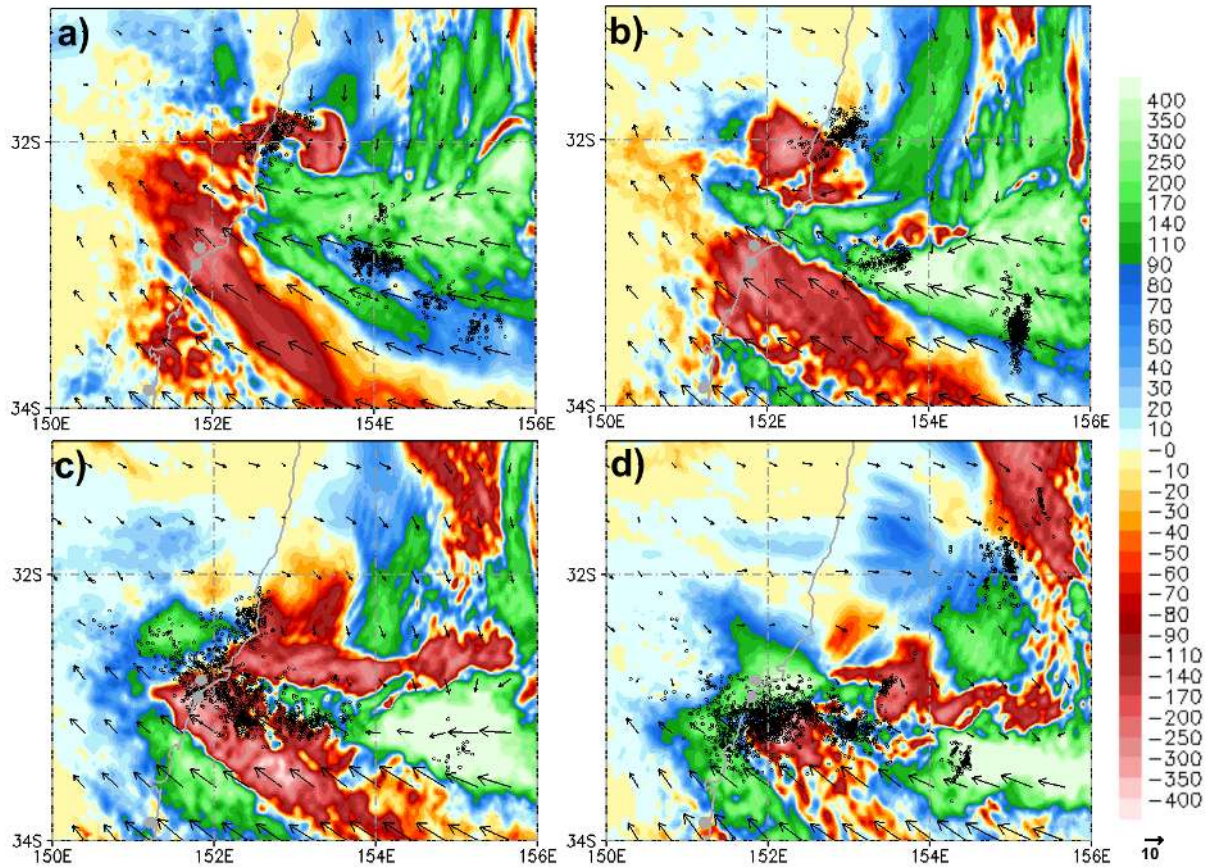
Figure 12: 3-hourly average MCAPE difference (J kg^{-1}, colour shades, JUN07a_BN -
JUN07a_skin) and 10 metre JUN07a_BN horizontal wind vectors (ms^{-1}, representative vector
in bottom right) for a) 1200 to 1500 UTC 7 June, b) 1500 to 1800 UTC, c) 1800 to 2100 UTC
7 June, and d) 2100 UTC 7 June to 0000 UTC 8 June. 3 hour total lightning strikes are
overlaid for periods 6 hours later than the MCAPE difference plot so the lightning periods are
a) 1800 to 2100 UTC 7 June, b) 2100 UTC 7 June to 0000 UTC 8 June, c) 0000 to 0300
UTC, and d) 0300 to 0600 UTC 8 June. In a) are the locations of representative observation
station Williamtown, Nobbys, and Sydney.

Author/s:
Chambers, CRS;Brassington, GB;Walsh, K;Simmonds, I

Title:
Sensitivity of the distribution of thunderstorms to sea surface temperatures in four Australian east coast lows

Date:
2015-10-01

Citation:
Chambers, C. R. S., Brassington, G. B., Walsh, K. & Simmonds, I. (2015). Sensitivity of the distribution of thunderstorms to sea surface temperatures in four Australian east coast lows. METEOROLOGY AND ATMOSPHERIC PHYSICS, 127 (5), pp.499-517. https://doi.org/10.1007/s00703-015-0382-4.

Persistent Link:
http://hdl.handle.net/11343/282722